

EXACT SOLUTIONS TO THE CANCER LASER ABLATION MODELING

LUISA CONSIGLIERI

ABSTRACT. The present paper deals with the study of the fluence rate over both healthy and tumor tissues in the presence of focal laser ablation (FLA). We propose new analytical solutions for the coupled partial differential equations (PDE) system, which includes the transport equation modeling the light penetration into biological tissue, the bioheat equation modeling the heat transfer and its respective damage. The present building could be the first step to the knowledge of the mathematical framework for biothermophysical problems, as well as the main key to simplify the numerical calculation due to its no cost. We derive exact solutions and simulate results from them. We discuss the potential physical contributions and present respective conclusions about (1) the validness of the diffusion approximation of the radiative transfer equation; (2) the local behavior of the source of scattered photons; (3) the unsteady-state of the fluence rate; and (4) the boundedness of the critical time of the thermal damage to the cancerous tissue. We also discuss some controversial and diverging hypotheses.

1. INTRODUCTION

Thermal ablation is a widely accepted therapy for denaturing proteins and then the destruction of tissue cells. It has been used both for the treatment of atrial fibrillation [45] or cancer [14, 26]. In the last decades, several energy sources have been applied (see [23, 18] and references therein), including radiofrequency [10, 6, 36, 16], microwave [5, 47], cryoablation [15, 2, 22], ultrasound [19], and laser [29, 46]. Focal Laser Ablation (FLA) is a minimally invasive procedure used to treat tumors by using laser energy to heat and destroy cancerous cells. Indeed, FLA is gaining acceptance as a safe option and effective alternative to surgical resection [37, 44, 41] and the references therein.

An ideal hyperthermia treatment is one that selectively destroys the diseased cells without damaging the surrounding healthy tissue. For this reason, it is still essential build analytical solutions to respond such selective targeting. The FLA model results from three distinct phenomena: conversion of laser light into heat, transfer of heat, and coagulation necrosis. It consists of the coupled partial differential equations (PDE) system which includes the diffusion approximation of the radiative transfer equation modeling the light penetration into biological tissue, the Pennes bioheat transfer equation modeling the heat transfer, and the Arrhenius burn integration modeling the dimensionless indicator of damage. The worldwide literature of the heat transfer on the

2020 *Mathematics Subject Classification.* Primary: 78-10; 80-10; Secondary: 34A05; 78A60; 92C05; 92C50.

Key words and phrases. Focal laser ablation (FLA); Pulsed laser ablation; tissue damage; Beer-Lambert law; exact solutions.

ablation modeling commonly considers the heat source as constant or of particular profile. In FLA, the heat source, the so-called absorbed optical power density, is induced by the conversion of laser light into heat and has a well-known linear relationship with the fluence rate. In the presence of this relationship, accurate knowledge of the fluence rate is the key feature for the mathematical framework.

For a light source acting as a cylindrical diffuser, the fluence rate is obtained in terms of zero-order modified Bessel functions [42, pp. 172-174]. Also other expressions exist (see, for instance, [24] and the references therein). For a single spherically symmetric point source emitting, we mention [31, 40, 42] and references therein. The laser beam has a crater-like shape, since the intensity is not constant across the beam width but decreases from the center towards the edge [48].

Some analytical solutions to the bioheat transfer problem are studied for RF ablation in multiregion domains [11, 7, 8]. We refer to [31] in which finite element model simulations of laser therapy are computed. For the skin surface in [25], the authors provide a theoretical study of the thermal wave effects in the bioheat transfer problem involving high heat flux incident with a short duration. For breast tumor thermal therapy in [19], the authors propose cylindrical ultrasound phased array with a multifocus pattern scanning strategy. For a spherical tumor in [36], the authors simulate the current density distribution when a 3D current density is generated by different multiple-straight needle electrode configurations. By using finite element modeling in [34], the authors analyze the photo-thermal heating with near-infrared radiation in the presence of intravenous blood injection or intratumorally injected gold nanorods. We refer to [9] the study of the endovenous laser ablation (EVLA), which stands for a similar technique to treat varicose veins by using laser energy to close off the affected veins.

One-dimensional, time-dependent models for the removal of material using a laser beam were published in [48] and the references therein. The thermal penetration differs with the laser system (Argon, Nd:YAG, and CO₂ [29]). Failure rates may depend on the design of the optical fibers. In [1], the authors show that the heat-affected zone is significantly reduced by using a short pulsed laser of the same average power (150 mW for 25 seconds) as compared to a CW laser source. Short pulsed lasers are being used in a variety of applications such as remote sensing, optical tomography, laser surgery, and ablation processes.

In the present work, we derive exact solutions and apply the resulting solutions under Nd:YAG and diode lasers for their wide application. We analyze the light source over different tissues and its tissue absorption under the Beer-Lambert (BL) law. We focus our attention on breast and prostate tumors that are common cancers worldwide diagnosed in women and men, respectively [13, 27].

The outline of the present work is as follows. We firstly describe the mathematical model in Section 2. In Section 3, we propose new exact solutions for the unknown functions under study. In Section 4, we apply the previous results to the fluence rate and temperature in the existence sections 4.1 and 4.3, respectively, and present some simulation in Section 4.2. Section 5 indicates the main interpretations and conclusions.

Finally, two Appendices are included to contain mathematical proofs relative to Section 4.

2. MATHEMATICAL FORMULATION

We assume the geometry of the laser–tissue system to be as illustrated in Figure 1. The laser applicator usually consists of an optical fiber (with radius r_f) incorporated within a catheter. The diameter of the optical fiber for medical applications varies between $200\ \mu\text{m}$ and $600\ \mu\text{m}$ [30], while the laser beam diameter is $2\ \text{mm}$ [1]. Thus, we may assume $r_f = 0.25\ \text{mm}$ [28].

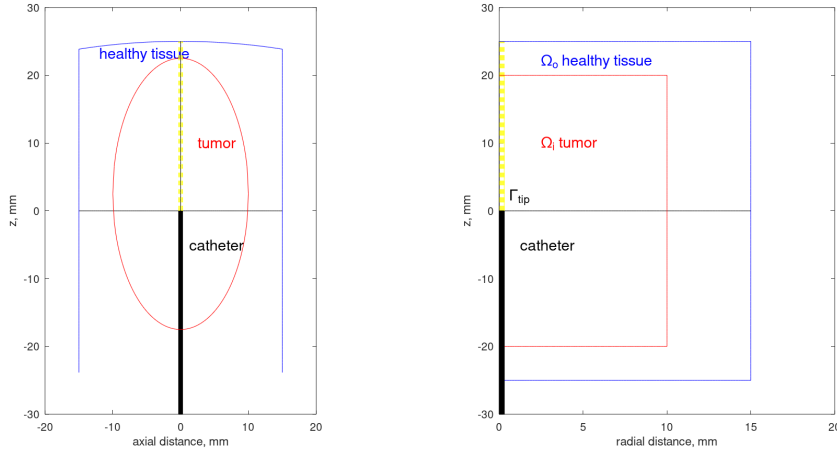


FIGURE 1. Schematic representations of the laser-tissue system: the laser emission tip $\Gamma_{\text{tip}} = \{(x, y) \in \mathbb{R}^2 : x^2 + y^2 < r_f^2\} \times \{0\}$, the light-emitting cylinder $]0; r_f[\times]0; L[$, the tumor $\Omega_i =]0; r_i[\times]-\ell; \ell[$, and the surrounding healthy tissue $\Omega_o = \{(x, y) \in \mathbb{R}^2 : x^2 + y^2 < r_i^2\} \times]\ell; L[\cup \{(x, y) \in \mathbb{R}^2 : r_i^2 < x^2 + y^2 < r_o^2\} \times]0; L[$. Left: Sagittal view. Right: Cylindrical coordinates (r, z) .

Both breast and prostate tumors can be modeled as ellipsoid (see [13, 28] and references therein). We assume the tumor Ω_i and surrounding healthy tissue Ω_o to be cylindrical with r_i and r_o being the inner and outer radius, respectively. Let us define the bidomain

$$\Omega = \text{int}(\overline{\Omega_i} \cup \Omega_o).$$

Mean breast and prostatic carcinoma sizes may vary in different ranges. We assume the inner radius $r_i = 1\ \text{cm}$. Although the primary goal is to destroy all malignant tissue, the surrounding nonmalignant tissue should be preserved. To evaluate this rim of surrounding tissue, the outer radius r_o will be determined such that the fluence rate vanishes. Indeed, the respective photons just "vanish" from the system due to the light reaching the system border is absorbed.

The laser light is emitted from the distal end of the fiber on an active length which is approximately half the tumor size [30, p. 82]. By this reason, the distal end is

assumed to be centered in the middle of the tumor, that is, the longitudinal coordinate is $-\ell < z < \ell$.

Three different instants of time are of reference: the temporal pulse width t_p (also known as pulse duration or pulse width, for short), the critical time t_{crit} , and the exposure duration t_{end} . The pulse width t_p is the time measured across a pulse, at its full width half maximum (FWHM). The critical time t_{crit} is introduced in Section 2.3. The exposure duration t_{end} consists of N pulse widths and $N - 1$ pulse-to-pulse intervals Δt (the so-called periods), which are ten times the pulse width [29].

2.1. Photon transport. The photon transport is governed by the diffusion approximation of the radiative transfer equation (see, for instance, [30, 42, 35])

$$\frac{1}{\nu} \frac{\partial \phi}{\partial t} - D \Delta \phi + \mu_a \phi = S \quad \text{in } \Omega \times]0; t_{\text{end}}[, \quad (1)$$

where:

- ϕ is the fluence rate [W m^{-2}];
- ν is the light velocity in the tissue [m s^{-1}], $\nu = c/n$, with the light velocity $c = 3 \times 10^8 \text{ m s}^{-1}$ and the relative refractive index n ;
- μ_a is the absorption coefficient [m^{-1}].

The diffusion coefficient is

$$D = \frac{1}{3(\mu_a + \mu'_s)}.$$

Here, the reduced scattering coefficient μ'_s [m^{-1}] is a function of the wavelength λ , which is normalized by the reference wavelength 500 nm,

$$\mu'_s = a \left(\frac{\lambda}{500} \right)^{-b}$$

where a and b are known constants [20]. The reduced scattering coefficient obeys $\mu'_s = (1 - g)\mu_s$, with g being the scattering anisotropy coefficient and μ_s being the scattering coefficient. The biological tissue is a strongly scattering media and then g ranges from 0.7 to 0.99 for most biological tissues [30]. The optical parameters of the tissue are known (cf. Table 1), which are assumed to be temperature independent [48]. The average of μ_a and μ'_s belong to the range 0–0.6 and 0–20 cm^{-1} , respectively.

TABLE 1. Average optical parameters for breast and prostate (tumor and healthy) tissues [20, 30, 40].

	μ_a [cm^{-1}]			a [mm^{-1}]	b	n
λ [nm]	810	980	1,064			
Breast tumor	0.08	0.07	0.06	2.07	1.487	1.4
Prostate tumor	0.12	0.11	0.1	3.36	1.712	1.4
Breast tissue	0.17	0.2	0.3	1.68	1.055	1.35
Prostate tissue	0.6	0.5	0.4	3.01	1.549	1.37

We consider that the beam divergence is negligible around the focus, and then the effects of the laser radiation in terms of the local absorption of light are according to the Beer–Lambert law [35]. The source of scattered photons S [W m^{-3}] represents the power injected in the unit volume, and it is given by

$$S(r, z, t) = \frac{\mu_s(\mu_t + g\mu_a)}{\mu_a + \mu'_s} E(r, t) \exp[-\mu_t z], \quad (2)$$

for $(r, z, t) \in]0; r_o[\times]0; L[\times]0; t_{\text{end}}[$. Here, the total attenuation coefficient is

$$\mu_t = \mu_a + \mu_s = \mu_a + (1 - g)^{-1} a(500/\lambda)^b, \quad (3)$$

and the planar irradiance, over the exposure duration t_{end} , is

$$E(r, t) = \frac{P_{\text{peak}}}{\pi r_f^2} \chi_{[0; r_f]}(r) \sum_{j=0}^{N-1} \chi_{[t_j; t_j + t_p]}(t), \quad (4)$$

with P_{peak} [W] standing for the maximum optical power output by the laser, each pulse time $t_j = j(t_p + \Delta t)$, and χ_I standing for the characteristic function over the interval I . The number of pulses is such that $N = (t_{\text{end}} + \Delta t)/(t_p + \Delta t)$.

The difference on relative refractive indices between tumor media and healthy tissue is positive, namely the tumor refractive index $n_0 = 1.4 > n_1$ (the refractive index of the medium of the transmitted ray). At the interfaces, where mismatched refractive indices occur, we may consider the Robin boundary conditions [3, 35]

$$-D \frac{\partial \phi}{\partial z} + \gamma_r \phi = -S_1 \quad \text{at } z = \ell; \quad (5)$$

$$-2D \frac{\partial \phi}{\partial r} + \gamma_r \phi = 0 \quad \text{at } r = r_i. \quad (6)$$

Here, the coefficient γ_r denotes a reflectance dependent function [42, 35], and $S_1(r, z) = g\mu_s/\mu_{\text{tr}} * E(r, t_p) \exp[-\mu_t z]$, with $\mu_{\text{tr}} = \mu_a + \mu'_s$ being the transport attenuation coefficient. Notice that the source of scattered photons $S = -\text{div}S_1 + S_2$, where $S_2(r, z) = \mu_s * E(r, t_p) \exp[-\mu_t z]$ and

$$S_1(r, z) = \frac{g}{\mu_t + g\mu_a} S(r, z, t_p). \quad (7)$$

The Robin boundary conditions (5)-(6) mean whenever light reaching the system borders some photons are reflected back into the system.

The remaining interfaces, $z = 0$ and $r = r_f$, are indeed mathematical boundaries and not tissue borders. Thus, we assume continuity of the fluence rate ϕ and its flux.

2.2. Heat transfer. The heat transfer due to the energy of light deposited is governed by the Pennes bioheat transfer equation that distinguishes from nonliving medium:

$$\rho c_p \frac{\partial T}{\partial t} - \nabla \cdot (k \nabla T) + c_b \omega_b (T - T_b) = q \quad \text{in } \Omega \times]0; t_{\text{end}}[, \quad (8)$$

where:

- T is the temperature [K];
- ρ is the density of the tissue [kg m^{-3}];

- ω_b represents the blood perfusion rate [$\text{kg m}^{-3} \text{s}^{-1}$] that occurs in the capillary bed.

In particular, the constant T_b represents the temperature of the blood (assumed to be 38°C), ρ_b and c_b denote the density and the specific heat capacity of the blood, respectively, and $c_b\omega_b$ accounts for the heat conducted in direction of the contribution of flowing blood to the overall energy balance, before the critical coagulation temperature. The blood perfusion rate ω_b may have a nonlinear temperature dependence [38]. Here, we assume ω_b that obeys the linear time dependence (11).

The specific heat capacity per unit mass c_p [$\text{J kg}^{-1} \text{K}^{-1}$] and thermal conductivity k [$\text{W m}^{-1} \text{K}^{-1}$] may be based on the following relationships [30, pp. 68-69]:

$$\begin{aligned} c_p &= 1550 + 2800 \frac{\rho_w}{\rho}; \\ k &= 0.06 + 0.57 \frac{\rho_w}{\rho}, \end{aligned}$$

where ρ_w denotes the density of the water.

The metabolism behavior is neglected due to its small contribution to the temperature response. Then, the laser light induced heat source q [W m^{-3}], the so-called absorbed optical power density, is governed by

$$q = \mu_a \phi. \quad (9)$$

We refer to [17, 21, 43] the thermal relaxation time in the conduction equation with both Fourier and non-Fourier effects, instead of considering the system (8)-(9). In the last years, the researchers keep proposing various alternatives to the benchmark work developed by Pennes. We may mention [12], and the references therein, in which a local thermal non-equilibrium bioheat model is studied.

2.3. Thermal damage to the tissue. Thermal laser-tissue interaction exhibits four phases: coagulation, vaporization, carbonization, and melting (vacuolation) [30, pp. 58-63].

A critical time t_{crit} , which corresponds to the dimensionless indicator of damage when it is equal to one: $\Omega(t_{\text{crit}}) = 1$, obeys the Arrhenius burn integration [38]

$$\frac{1}{A} = \int_0^{t_{\text{crit}}} \exp \left[-\frac{E_a}{RT(r, z, \tau)} \right] d\tau, \quad (10)$$

where R is the universal gas constant ($8.314 \text{ J mol}^{-1} \text{K}^{-1}$), A is the frequency factor [s^{-1}] (also known as Arrhenius factor), and E_a is the activation energy for the irreversible damage reaction [J mol^{-1}].

The linear behavior of the blood perfusion rate ω_b is defined by

$$\omega_b(t) = \omega_0(1 - t/t_{\text{crit}}), \text{ for } 0 \leq t \leq t_{\text{crit}}, \quad (11)$$

with $\omega_0 = \rho_b w$ denoting the initial value of the blood perfusion, where w denotes the volumetric flow [s^{-1}]. The blood perfusion rate ω_b is set to zero if there is no blood perfusion, which is the case for $t > t_{\text{crit}}$.

3. ANALYTICAL SOLUTIONS

Our objective is to build exact solutions that fit, in particular, the physiological problem under study,

$$\tau \partial_t u - \alpha \Delta u + Bu = f, \quad (12)$$

via the separable variable method, in cylindrical coordinates *i.e.* at the position (r, z) and the time t . Using Bernoulli–Fourier technique, we have

$$(\tau X'(t) + [-\alpha(\beta + \eta^2) + B]X(t)) R(r)Z(z) = f(r, z, t), \quad (13)$$

where the constants $\beta, \eta \in \mathbb{R}$ are arbitrary,

Radiative transfer: $\tau = 1/\nu$, $\alpha = D$, $B = \mu_a$ and $f = S$ in Subsection 2.1;

Heat transfer: $\tau = \rho c_p$, $\alpha = k$, $B = c_b \omega_b(t)$ and $f = q$ in Subsection 2.2.

The functions X , Z and R are elementary solutions to the system of ordinary differential equations (ODE)

$$\begin{cases} X'(t) = \zeta X(t) \\ Z''(z) = \eta^2 Z(z) \\ (rR'(r))' = \beta rR(r) \end{cases} \quad (14)$$

for some time parameter $\zeta \in \mathbb{R}$. The nonconstant behavior of ω_b (cf. (11)) does not invalidate the application of this technique in determining an analytical solution for the heat transfer.

Firstly, a particular solution is available due to the Duhamel principle (for details, see [9] and the references therein). Secondly, let us seek for elementary solutions of the ODE system (14).

The first-order ODE in (14) admits the elementary solution

$$X(t) = \exp\left[\int_0^t \zeta(s) ds\right], \quad t > 0. \quad (15)$$

The second-order ODE in (14), with constant coefficients, admits the elementary solutions

$$Z(z) = \exp[\pm \eta z], \quad z \in \mathbb{R}. \quad (16)$$

The second-order ODE in (14), with nonconstant coefficients, admits the Bessel functions of first and second kind and order 0, respectively, $J_0(\sqrt{|\beta|r})$ and $Y_0(\sqrt{|\beta|r})$ if $\beta < 0$; or the modified Bessel functions of first and second kind and order 0, respectively, $I_0(\sqrt{\beta}r)$ and $K_0(\sqrt{\beta}r)$ if $\beta > 0$ [33]. If $\beta = 0$, the elementary solutions reduce to $R(r) = \log[r]$ and the unity function.

Then, a general solution solving the homogeneous equation (13) ($f = 0$) is available by the above elementary solutions, if

$$\tau \zeta + B = \alpha(\beta + \eta^2). \quad (17)$$

Finally, we analyze the PDE (12) at the period of time $0 < t_j + t_p < t < t_{j+1}$, for any $j = 0, \dots, N-1$. This case will describe the homogeneous problem, which is governed without source ($f = 0$), at one pulse-to-pulse interval Δt . For the sake of simplicity, we denote the initial instant of time $t_j + t_p$ by t_0 throughout this subsection.

For the initial condition $u(r, z, t_0) = u_0 Z(\eta; z)$, where $Z(\eta; z)$ denotes a linear combination of the elementary solutions Z given as in (16), we apply the principle of superposition [33, Chapter 3-4] to obtain the solution in the form of the Fourier–Bessel series

$$u(r, z, t) = \sum_{m=1}^{\infty} c_m J_0(b_m r) Z(\eta; z) \exp[\zeta_m(t - t_0)] \quad (18)$$

that satisfies the homogeneous PDE (12) ($f = 0$) in a solid cylinder ($0 < r < a$) with finite length L . The zero-order Bessel function of the second kind, Y_0 , is excluded from the solution, because the region includes the origin $r = 0$ where Y_0 becomes infinite.

We adapt the homogeneous problems for heat equation ($B = 0$) in (r, z, t) variables [33, pp. 127-131], namely Example 3-9 for a hollow cylinder of finite length and Example 3-10 for a solid cylinder of semi-infinite length.

To determine the coefficients c_m , we multiply both sides of (18) by $r J_0(b_n r)$ and integrate over the section of the cylinder, obtaining

$$u_0 \int_0^a r J_0(b_n r) dr = c_n \int_0^a r J_0^2(b_n r) dr.$$

In the left hand side, we used the initial condition and in the right hand side, we apply the orthogonality relationship of the eigenfunctions

$$\int_0^a r J_0(b_m r) J_0(b_n r) dr = \delta_{m,n} \int_0^a r J_0^2(b_n r) dr \quad (19)$$

where $\delta_{m,n}$ is the Kronecker delta and the eigenvalues b_m are determined by the boundary condition.

For any $a, b > 0$, by integration we have [33, Appendix IV]

$$\begin{aligned} \int_0^a r J_0(br) dr &= \frac{a}{b} J_1(ba); \\ \int_0^a r J_0^2(br) dr &= \frac{a^2}{2} (J_0^2(ba) - J_{-1}(ba) J_1(ba)). \end{aligned}$$

Recall that $W_{-1}(a) = -W_1(a)$ for any Bessel function of zero order $W = J_0, Y_0, K_0, I_0$.

Then, the complete solution is

$$u(r, z, t) = \sum_{n=1}^{\infty} u_0 \frac{2}{b_n a} \frac{J_1(b_n a)}{J_0^2(b_n a) + J_1^2(b_n a)} J_0(b_n r) Z(\eta; z) \exp[\zeta_n(t - t_0)]. \quad (20)$$

4. RESULTS

We focus on the study of the analytical solution for the fluence rate ϕ in this section. We derive an exact solution in Section 4.1 and its applicability in Section 4.2. This section ends with some considerations for the temperature and respective tissue damage in Section 4.3.

4.1. **Exact solution for the fluence rate.** The time parameter in (17) is

$$\zeta = \nu(D\mu_t^2 - \mu_a) = \frac{c}{n} \left(\frac{(\mu_a + (1-g)^{-1}a(500/\lambda)^b)^2}{3(\mu_a + a(500/\lambda)^b)} - \mu_a \right). \quad (21)$$

We denote ζ by ζ_{in} in the tumor, and ζ_{out} in the healthy tissue. According to Table 1, $\zeta_{\text{in}} > 0$.

For $0 \leq r \leq r_f$, $0 \leq z \leq \ell$ and $0 \leq t < t_p$, the transient solution of (1)-(2) is

$$\phi_f(z, t) \equiv \frac{S(r_f, z, 0)}{D\mu_t^2 - \mu_a} (\exp[\zeta_{\text{in}}t] - 1). \quad (22)$$

Hereafter, let us set

$$S_{\text{in}} = \frac{S(r_f, 0, 0)}{D^{(i)}(\mu_t^{(i)})^2 - \mu_a^{(i)}}, \text{ for } i = \text{inner}. \quad (23)$$

Next, let us consider the solution of (1)-(2), at two pulses, $]0; t_p[$ and $]t_1; t_1 + t_p[$ and the period between them $]t_p; t_1[$. For the general pulse width $]t_j; t_j + t_p[$ and the period $]t_j + t_p; t_{j+1}[$, we proceed *mutatis mutandis*.

For these two cases, let us extend the fluence rate ϕ to the entire multidomain.

Case $0 < t < t_p$: The fluence rate ϕ , as given in (22)-(23), verifies the initial condition $\phi(t = 0) = 0$. Moreover, the source S is a discontinuous function as defined in (2)-(4). Indeed, S can be neglected for $z > \ell$, as mentioned in Section 4.2. Hence, we consistently consider $\phi = 0$ if $z > \ell$.

For $r_f < r \leq r_o$ and $0 \leq z \leq \ell$, by the interface continuity condition at $r = r_f$ and the boundary condition (5) at r_i , we may extend ϕ as

$$\begin{aligned} \phi(r, z, t) &= R_1(r) \exp[-\mu_t z] + R_3(r) \exp[-\mu_t z + \zeta_{\text{in}}t] & \text{if } r_f < r \leq r_i; \\ &= R_2(r) \exp[-\mu_t z] + R_4(r) \exp[-\mu_t z + \zeta_{\text{in}}t] & \text{otherwise.} \end{aligned}$$

The existence of R_1 and R_3 rely on Appendices A.1 and A.2, respectively, and R_2 and R_4 are in accordance with Appendix B. Noting that the fluence rate ϕ verifies the initial condition $\phi(t = 0) = 0$, then $R_1 \equiv -R_3$. This means that $S = 0$ for $r > r_f$ and we consistently might consider $\phi = 0$ either $r > r_f$ or $z > \ell$, if $0 \leq t < t_p$. As we do not expect a zero fluence rate at $t = t_p$, we assume discontinuous ϕ in time.

The correspondent parameters are $\beta_1(0)$, $\beta_1(\zeta_{\text{in}})$ with β_1 being defined in (A.2), and $\beta_2(0)$, $\beta_2(\zeta_{\text{in}})$ with β_2 being defined in (B.1). In particular, we have

$$\beta_2(\zeta_{\text{in}}) = \left(\frac{\mu_a^{(o)} + a^{(o)}(\lambda/500)^{-b^{(o)}}}{\mu_a^{(i)} + a^{(i)}(\lambda/500)^{-b^{(i)}}} - 1 \right) (\mu_t^{(i)})^2 - (\mu_a^{(i)} - \mu_a^{(o)}) / D^{(o)},$$

where the superscripts (i) and (o) stand for inner and outer regions, respectively.

For $-\ell < z < 0$, the continuity of the fluence rate ϕ and the requirement of (17) being satisfied imply the symmetry of ϕ relative to $z = 0$.

Case $t_p \leq t < t_1 = t_p + \Delta t$: In this one pulse-to-pulse interval Δt , we seek for a solution such that satisfies the homogeneous PDE (1) and the initial condition $\phi_f(z, t_p)$. Moreover, the solution should decrease in time, with the time parameter ζ being defined in (17). The principle of superposition now guarantees that the complete solution is constructed as (20), taking $\eta = -\mu_t$ into account.

For $0 \leq r \leq r_f$ and $0 \leq z \leq \ell$, we consider the Fourier–Bessel series

$$\phi(r, z, t) = u_0 \sum_{n=1}^{\infty} \frac{2}{b_n a} \frac{J_1(b_n a)}{J_0^2(b_n a) + J_1^2(b_n a)} J_0(\sqrt{|\beta_n|} r) \exp[-\mu_t z + \zeta_n(t - t_p)]. \quad (24)$$

The initial constant $u_0 = \phi_f(0, t_p) = S_{\text{in}}(\exp[\zeta_{\text{in}} t_p] - 1)$, a denotes the radius correspondent to the under study region of the multidomain, and $b_n = \sqrt{|\beta_n|}$.

For $0 \leq r \leq r_f$ and $\ell \leq z \leq L$, the function ϕ may be given by

$$\phi(r, z, t) = u_0 \sum_{n=1}^{\infty} \frac{2}{b_n a} \frac{J_1(b_n a)}{J_0^2(b_n a) + J_1^2(b_n a)} J_0(\sqrt{|\beta_n|} r) Z_\ell Z_n(z) \exp[\zeta_n(t - t_p)],$$

where

$$Z_n(z) = \exp[-\mu_t^{(i)} \ell] \frac{\sinh[\eta_n(L - z)]}{\sinh[\eta_n(L - \ell)]}.$$

if the parameters η_n are determined by (17), that is, the sequence of parameters verify $\eta_n^2 = \left(\zeta_n/\nu + \mu_a^{(o)}\right) / D^{(o)} - \beta_n > 0$, for $o = \text{outer}$, or

$$Z_n(z) = \exp[-\mu_t^{(i)} \ell] \frac{\sin[\eta_n(L - z)]}{\sin[\eta_n(L - \ell)]},$$

if $\eta_n^2 = -\left(\left(\zeta_n/\nu + \mu_a^{(o)}\right) / D^{(o)} - \beta_n\right) > 0$.

The constant Z_ℓ is determined by the Robin boundary condition (5) on the function ϕ at $z = \ell$, taking (7) into account.

For the remaining multidomain, we may proceed analogously considering the principle of superposition [33].

4.2. Profiles. In this section, we simulate results by the derived exact solution. The presented calculations use Octave software, under the optical parameters in Table 1.

Different wavelengths are used in this work to simulate two types of lasers: Q-switched short pulsed Nd:YAG laser operating at a wavelength of 1064 nm and diode short pulsed laser operating at a wavelength of 810 nm and 980 nm. Also the values of the pulse widths vary. They can range from 500 ms to 2 ms in Nd:YAG lasers [29], from nanosecond ($1 \text{ ns} = 1 \times 10^{-9} \text{ s}$) to picosecond ($1 \text{ ps} = 1 \times 10^{-12} \text{ s}$) in most diode lasers and of femtosecond order ($1 \text{ fs} = 1 \times 10^{-15} \text{ s}$) in free-electron lasers.

We begin by analyzing the light absorption of the tissues according to the BL law. Figure 2 illustrates the linear and semi-log steady-state profiles of S for these operating wavelengths, under optical values of the carcinoma-adipose breast and tumor-healthy prostate tissues according to Table 1.

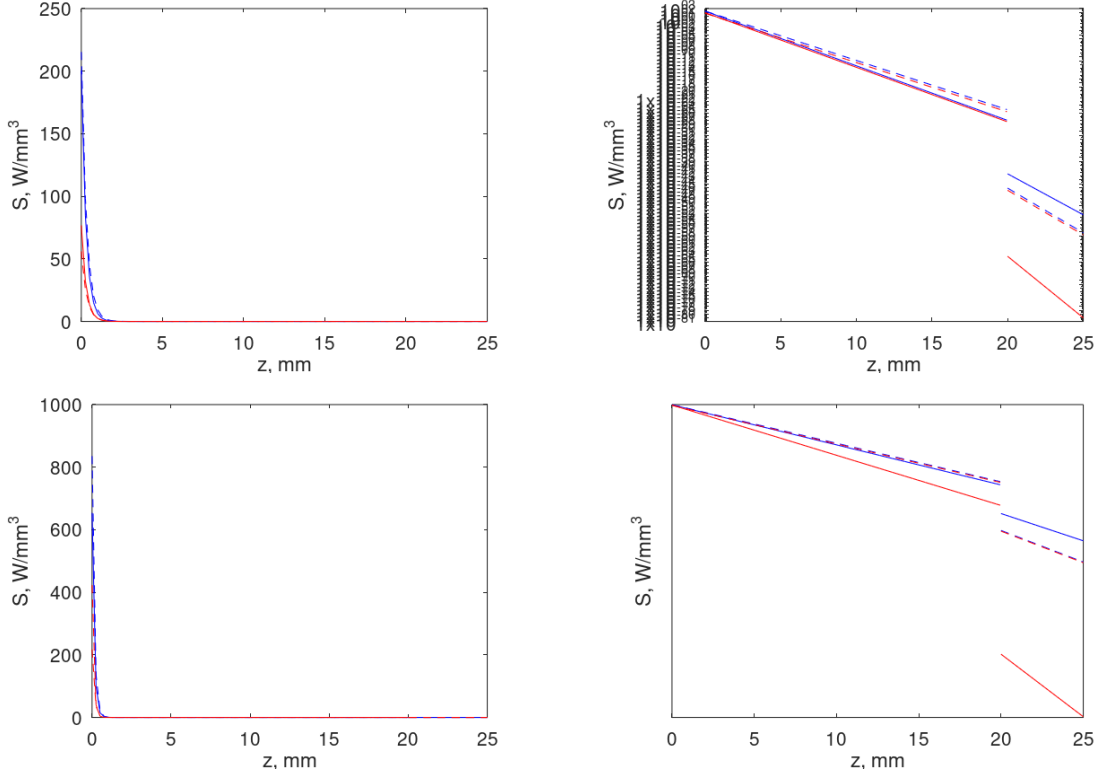


FIGURE 2. Graphical representations of the source S for the wattage set at 5 W (in blue): with wavelengths of 810 nm (solid line) and 980 nm (dashed line) and at 1.3 W (in red): with wavelengths of 980 nm (dashed line) and 1064 nm (solid line). (a) Plot with linear axes of the breast source. (b) Plot using a logarithmic scale for the y -axis of the breast source. (c) Linear plot of the prostate source. (d) Semilog plot of the prostate source. For details see Table 2.

At the tip $z = 0$, the source $S(0, 0, t_p)$ has its maximum values according to Table 2.

TABLE 2. Source values S at $z = 0$ (maximum), and at the discontinuity $z = \ell$ [W mm^{-3}].

λ [nm]	810	980	980	1,064
P_{peak} [W]	5	5	1.3	1.3
Maximum breast tumor	198	214	56	77
Minimum breast tumor	9.5e-28	6.8e-25	1.8e-25	3.9e-28
Maximum adipose breast	4.4e-42	6.3e-46	1.6e-46	3.1e-64
Maximum prostate tumor	647	828	215	420
Minimum prostate tumor	6.6e-62	2.2e-59	5.7e-60	2.7e-78
Maximum healthy prostate	2.6e-86	6.6e-100	1.7e-100	6.8e-200

We emphasize that the source S does not have expression in the outer region correspondent to the healthy tissue. Then, we may neglect the source S for $z > \ell$. For instance, at the wattage set at 5 W (in blue), with wavelength of 810 nm (solid line), we have $S(0, 20, t_p) \simeq 10^{-27} \text{ W mm}^{-3}$ for the breast tumor border and $S(0, 20, t_p) \simeq 10^{-42} \text{ W mm}^{-3}$ for the adipose breast border.

The fluence rate ϕ has different graphical representations displayed in Figure 3, at diode pulse width $t_p = 1 \times 10^{-11} \text{ s}$. Figure 3 shows distributions of ϕ for breast in (a) and prostate in (c), as function of the radius r , at the different operating systems. Figure 3 (b) shows distributions of ϕ for breast for the wattage set at 1.3 W and at a wavelength of 980 nm corresponding to the red dashed line in (a). Figure 3 (d) shows distributions of ϕ for prostate for the wattage set at 5 W and at a wavelength of 810 nm corresponding to the the blue solid line in (b).

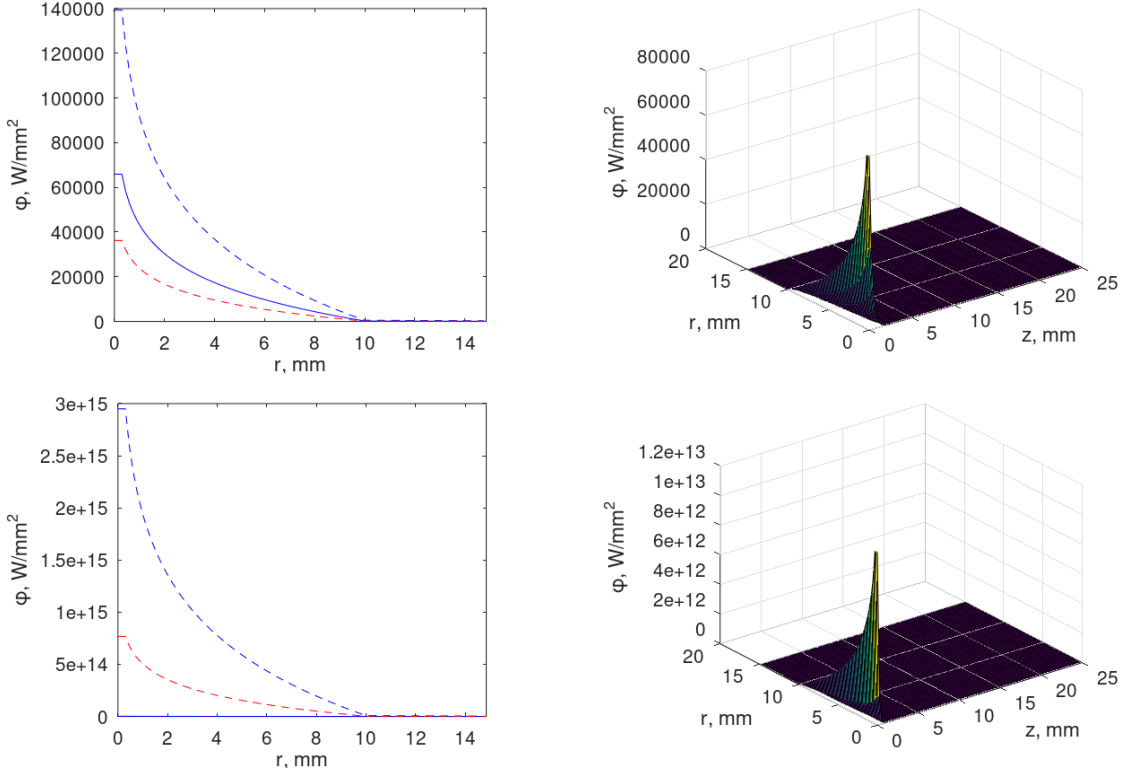


FIGURE 3. (a) Breast radial graphical representations of the fluence rate ϕ for the wavelength of 810 nm and wattage set at 5 W (blue solid line) and for 980 nm and wattage set at 5 W (blue dashed line) and at 1.3 W (red dashed line). (b) Plot for the tumor-adipose breast tissue for the wavelength of 980 nm and wattage set at 1.3 W. (c) Prostate radial graphical representations of the fluence rate ϕ as in (a). (d) Plot for the tumor-healthy prostate tissue for the wavelength of 810 nm and wattage set at 5 W.

At the referred values of pulse width in the order of ms for Nd:YAG, the fluence rate ϕ does not fit a coherent result. Indeed, the value of $\exp[\zeta_{in} t_p] \gg 1e + 304$. This drawback is due to the presence of the light velocity ν in the tissue.

Next, Figure 4 displays graphical representations of the fluence rate ϕ , at diode pulse width $t_p = 1.0$ ps. Figure 4 shows distributions of ϕ for breast in (a) and prostate in (c), as function of the radius r , at the different operating systems. Again, the result relative to the situation of wavelength of 1.064 nm is excluded by the same reason as before. Figure 4 (b) and (d) show distributions of ϕ for breast and prostate, respectively, for the wattage set at 1.3 W and at a wavelength of 980 nm corresponding to the red dashed line in (a) and (b).

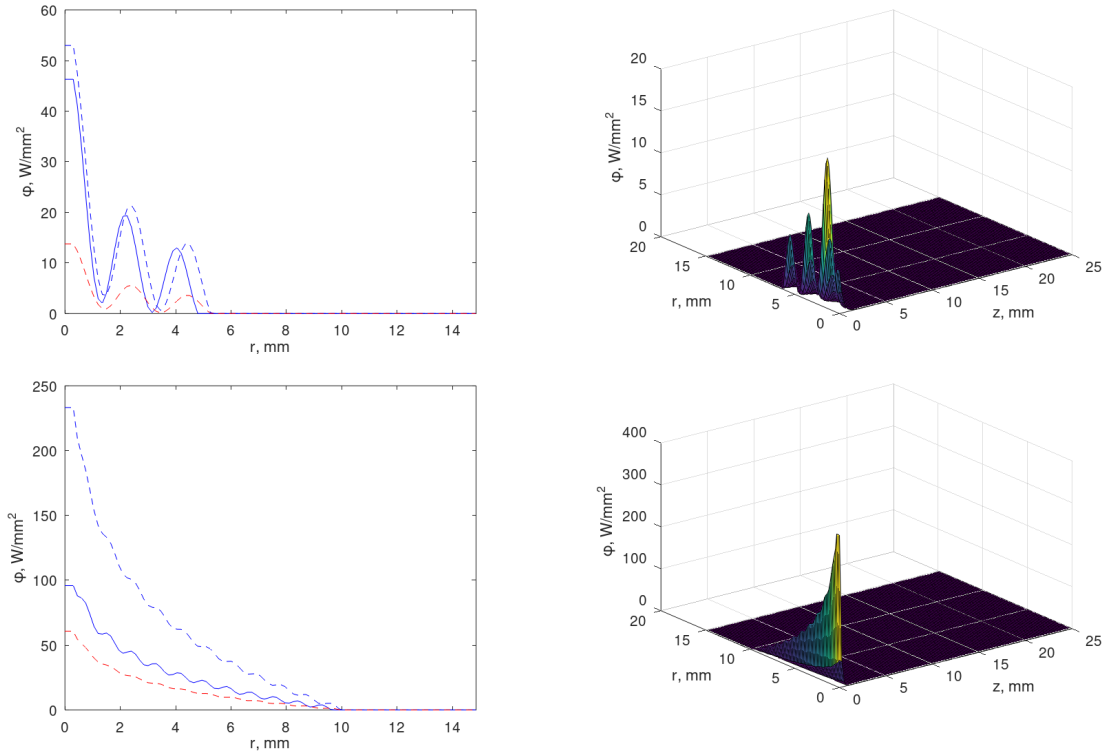


FIGURE 4. (a) Breast radial graphical representations of the fluence rate ϕ for the wavelength of 810 nm and wattage set at 5 W (blue solid line) and for 980 nm and wattage set at 5 W (blue dashed line) and at 1.3 W (red dashed line). (b) Plot for the tumor-adipose breast tissue for the wavelength of 980 nm and wattage set at 1.3 W. (c) Prostate radial graphical representations of the fluence rate ϕ as in (a). (d) Plot for the tumor-healthy prostate tissue for the wavelength of 980 nm and wattage set at 1.3 W.

At the temporal pulse width t_p , the fluence rate does not rapidly decrease with distance from the tip surface, which implies that the the Joule effect heating is generated along the r -direction. Also in Figure 4 (b) and (d), the slopes of curves in

the z -direction illustrate that the fluence rate ϕ is locally concentrated on the origin relative to the tip surface. Distributions of the fluence rate over time until t_{end} are subject of study in forthcoming work. The analysis of the behavior of the outer radius r_o is still an open problem.

4.3. Temperature and tissue damage. The time dependent parameter ζ in (17) is

$$\zeta(\beta; t) = (\rho c_p)^{-1} (k(\beta + \mu_t^2) - c_b \rho_b w (1 - t/t_{\text{crit}})).$$

We set

$$\zeta_1(\beta; t) = \begin{cases} \zeta(\beta; 0) & \text{for } t < t_p \\ \zeta(\beta; t) & \text{for } t_p \leq t < t_{\text{crit}} \\ \zeta(\beta; t_{\text{crit}}) & \text{for } t \geq t_{\text{crit}} \end{cases}$$

under the parameter β , namely $\beta = 0$, $\beta = \beta_1$ or $\beta = \beta_2$, according to Appendices A and B. Notice that ζ increases as function of time and ζ_1 obeys $\zeta(\beta; 0) \leq \zeta_1(\beta, t) \leq \zeta(\beta; t_{\text{crit}})$, for all $t > 0$. For the sake of simplicity, we write the constant $\zeta_0 = \zeta(0; 0)$. According to Table 3, we can calculate ζ_0 in the tumors (cf. Table 4).

TABLE 3. Average thermal parameters for blood and for breast and prostate (tumor and healthy) tissues [19, 28].

	unit	blood	breast tumor	prostate tumor	gland	fatty tissue
ρ	kg m ⁻³	1060.00	1000.00	999.00	1041.00	920.00
ω_0	kg m ⁻³ s ⁻¹		0.5	0.416	0.54	0.32

The breast tumor is commonly located in the gland tissue. If the breast tumor is located in the adipose tissue, the healthy tissue will exhibit lower density and blood perfusion values than ones of the tumor, as for the prostate values (cf. Table 3). Also, the density of any tumor varies from lower values at a primary stage and then increases at very high values.

TABLE 4. Values for parameter ζ_0 at different wavelengths.

λ [nm]	breast	prostate
810	1.7e+3	7.9e+3
980	1.4e+3	7.3e+3
1,064	1.7e+3	1.2e+4

Thanks to the Duhamel principle (for details see [9]), the solution of (8)-(9) is, for $0 \leq r \leq r_f$ and $0 \leq z \leq \ell$,

- if $0 \leq t < t_p$:

$$\begin{aligned} T(r, z, t) &= T_b + \frac{\mu_a}{\rho c_p} \frac{S(r_f, z, 0)}{D\mu_t^2 - \mu_a} \int_0^t (\exp[\zeta_{in}s] - 1) \exp[\zeta_0(t-s)] ds \\ &= T_b + \mu_a S_{in} \exp[-\mu_t z] \left(\frac{\exp[\zeta_{in}t] - \exp[\zeta_0t]}{\rho c_p (\zeta_{in} - \zeta_0)} + \frac{1 - \exp[\zeta_0t]}{k\mu_t^2 - c_b \rho_b w} \right); \end{aligned}$$

- if $t \geq t_p$:

$$T(r, z, t) = T(r_f, z, t_p) + \frac{\mu_a}{c_p \rho} \int_{t_p}^t \phi(r_f, z, s) \exp\left[\int_0^{t-s} \zeta_1(0; \tau) d\tau\right] ds.$$

We may extend the temperature T to the entire multidomain, by proceeding as in Section 4.1.

To evaluate the thermal damage, we need to estimate t_{crit} . From (10), we have

$$\frac{1}{A} \exp\left[\frac{E_a}{RT_{max}}\right] \leq t_{crit} \leq \frac{1}{A} \exp\left[\frac{E_a}{RT_{min}}\right], \quad (25)$$

where

$$T_{max} = \sup_{\Omega \times]0, t_{crit}[} T; \quad T_{min} = \inf_{\Omega \times]0, t_{crit}[} T.$$

The minimum temperature $T_{min} = T_b$ and t_{crit} obeying (25) verifies

$$t_{crit} \leq \frac{1}{A} \exp\left[\frac{E_a}{RT_b}\right]. \quad (26)$$

Typical values for prostate tumor are $E_a = 5.67 \times 10^5 \text{ J mol}^{-1}$ and $A = 1.7 \times 10^{91} \text{ s}^{-1}$ [18]. Based on these values, (26) infers that t_{crit} obeys the upper bound $t_{crit} \leq 9.9 \times 10^3 \text{ s} \sim 2.75 \text{ h}$. As commonly accepted, the maximum temperature with respect to produce complete in situ destruction of tissue is $T_{max} = 50^\circ \text{C}$. Then, t_{crit} similarly obeys the lower bound $t_{crit} \geq 2.8871 \text{ s}$.

5. DISCUSSION AND CONCLUSIONS

We firstly emphasize that the validness of the diffusion approximation of the radiative transfer equation (1) is true. Some important findings include the fact that the criterion $\mu_a \ll \mu'_s$ can not be disregard in the validity of the stationary diffusion approximation as stated but not proven in [42] for any geometric domain: plane [42, Section 6.4.1], spherical with isotropic point source [42, Section 6.4.2], or cylindrical [42, Section 6.4.3]. The criterion $\mu_a \ll \mu'_s$ in the validity is precisely quantified in [3] as $\mu_a/\mu'_s \sim 1/100$. According to Table 1, we calculate μ_a/μ'_s (cf. Table 5).

TABLE 5. Values for μ_a/μ'_s at different wavelengths.

λ [nm]	breast tumor	breast tissue	prostate tumor	prostate tissue
810	7.9e-03	1.7e-02	8.2e-03	4.2e-02
980	9.2e-03	2.4e-02	1.0e-02	4.7e-02
1,064	8.9e-03	4.0e-02	1.1e-02	4.3e-02

The criterion is verified by all values. Although some of the values are indeed greater, they verify $\mu_a/\mu'_s \sim 1/100$. In contrast in [4], the authors argue that the δ -Eddington approximation to the Boltzmann transport equation provides small percentage error if $\mu'_s/\mu_a \sim 100$.

Our first finding is that the source S does not reach the outer region correspondent to the healthy tissue, when the laser emission tip surface is located at the middle of the tumor, for one pulse width. Figure 2 and Table 2 confirm the local behavior of the source S . Its longitudinal discontinuity shown in Figure 2 (b) and (d) is a consequence of the tissue dependence on the optical values. Therefore, if the laser tip is fix at the center of the tumor, its action is local. Then, a moving tip, as used in EVLA [9], should be object of study in future research in order to find out if a better performance will be provided.

The relationship (17) implies some others conclusions about the diffusion approximation of the radiative transfer equation (1). If source of scattered photons S is given in function of the effective attenuation coefficient $\mu_{\text{eff}} = \sqrt{3\mu_a(\mu_a + \mu'_s)}$ [31], the relationship (17) reads $\zeta/\nu + \mu_a = D\mu_{\text{eff}}^2 = \mu_a$. This means that the fluence rate will be steady-state, because $\zeta = 0$. In [35], the author presents a detailed analytical solution of the diffuse radiant fluence rate for time-independent searchlight problem on flat-slab and semi-infinite geometries, under homogeneous Dirichlet conditions, by using the Green's function method. Also, the author refers some inaccuracies of the diffusion approximation.

In Section 4.1, we derive the fluence rate ϕ as a solution of the diffusion approximation of the radiative transfer equation (1). Its simulations, throughout the inlet region, originated by the tumor, and the outlet region, originated by the healthy tissue, are illustrated in Figures 3 and 4, having different pulse widths.

On the one hand, we observe different behaviors occur at different pulse width values by comparing Figures 3 and 4, which suggest that there are values of the pulse width that blow up the exponential function, namely at pulse widths $t_p = 10$ ps or above. However, at pulse widths of order ps we may conclude that a further study of the time-dependent searchlight problem is a priority.

On the other hand, the present results in Figure 4 (a) and (c) suggest that power alone is a stronger contributor of the profiles magnitude than wavelengths. We observe that Figure 3 (c) for the prostate tissue indicates that it is the wavelength the main contributor of the profiles magnitude. However, taking into account the previous comment about the comparison between Figures 3 and 4, we discard the last observation in order to avoid ambiguities and erroneous conclusions.

Our last conclusion is that the treatment should have a moving focal point with short exposure time $t_{\text{end}} = t_{\text{crit}}$ to preserve the healthy tissue. We emphasize that to evaluate t_{crit} , as defined in Section 4.3 by the Arrhenius burn integration (10), is based on the dependence of the parameters A or E_a . A breaking point for either A or E_a is reported in [39], at $T = 54^\circ\text{C}$, which is greater than 50°C (known as the maximum temperature with respect to produce complete in situ destruction of tissue). To produce the complete cure of the patient at a least treatment time (for instance $t_{\text{crit}} = 2.8871\text{ s}$, for prostate tumor) is the desired objective.

To the study of the heat exchange problem for ablation performed in biomedical sciences, it is important that its source, the absorbed optical power density (9), be analytically precised. The various equations in the present paper allow to calculate the light fluence rate as a function of (r, z, t) , within different regions in space. We apply them to breast and prostate tumors, but they may be applied to any kind, by recurring to the optical and thermal properties of the tissue in study. According to the experimental methods, we set higher optical values for the tumor tissue than ones of the healthy, but our results may be replicated to inverse optical values.

Data availability. The data supporting presented results is publicly available in the repository: LuisaConsiglieri/FocalLaserAblationStudy (2025).

<https://doi.org/10.5281/zenodo.14993810>

Acknowledgements. Grateful thanks to Daniel Pfaller for his comments on the laser modeling.

APPENDIX A. EXTENDING INSIDE THE TUMOR

Let us consider

$$\phi(r, z, t) = R(r_f) \exp[-\mu_t z + \zeta t],$$

where $R(r_f)$ is a positive constant, which stands for

- the particular solution of (1)-(2), if $\zeta = 0$;
- the general solution of (1)-(2), if $\zeta = \nu(D\mu_t^2 - \mu_a)$ (or $\zeta = \zeta_{\text{in}}$, cf. (21)).

For $r_f < r \leq r_i$, we seek a function in the form

$$\phi(r, z, t) = R_1(r) \exp[-\mu_t z + \zeta t], \quad (\text{A.1})$$

with R_1 being a solution to the second-order ODE in (14), with nonconstant coefficients, with parameter β_1 verifying

$$\beta_1(\zeta) = \left(\zeta/\nu + \mu_a^{(i)} \right) / D^{(i)} - (\mu_t^{(i)})^2 \quad \text{for } i = \text{inner}. \quad (\text{A.2})$$

A.1. Particular solution. In this Section, β_1 reduces to

$$\beta_1 = \mu_a^{(i)} / D^{(i)} - (\mu_t^{(i)})^2 < 0.$$

According to Table 1, the constant β_1 is negative.

Using the continuity condition on the function ϕ at $r = r_f$, we have

$$R_1(r) = C_1 J_0(\sqrt{|\beta_1|}r) + \frac{R(r_f) - C_1 J_0(\sqrt{|\beta_1|}r_f)}{Y_0(\sqrt{|\beta_1|}r_f)} Y_0(\sqrt{|\beta_1|}r), \quad \text{for } C_1 \in \mathbb{R}. \quad (\text{A.3})$$

The involved constant C_1 in (A.3) may be determined by the continuity condition on the flux

$$C_1 J_1(\sqrt{|\beta_1|} r_f) + \frac{R(r_f) - C_1 J_0(\sqrt{|\beta_1|} r_f)}{Y_0(\sqrt{|\beta_1|} r_f)} Y_1(\sqrt{|\beta_1|} r_f) = 0. \quad (\text{A.4})$$

Applying the wronskian relationship (see [33, p. 672] and [32, pages 360 and 375])

$$J_1(\beta r) Y_0(\beta r) - Y_1(\beta r) J_0(\beta r) = \frac{2}{\pi \beta r}, \quad (\text{A.5})$$

for $\beta = \sqrt{|\beta_1|} > 0$, we may compute (A.4), concluding

$$C_1 = -\frac{\pi}{2} \sqrt{|\beta_1|} r_f R(r_f) Y_1(\sqrt{|\beta_1|} r_f).$$

A.2. General solution. Notice that the relationship (21) between the parameters ζ and μ_t leads $\beta_1 = 0$, then $R_1(r) = R(r_f) - \beta_0 \log[r/r_f]$, which verifies $R_1(r_f) = R(r_f)$. Here, b_0 is a positive constant determined by the Robin boundary condition (6), namely it is given by

$$b_0 = \frac{\gamma_r}{\gamma_r \log[r_i/r_f] - 2D/r_i} R(r_f).$$

APPENDIX B. EXTENDING OUTSIDE THE TUMOR ($z < \ell$)

In the tumor, let us consider the general solution

$$\phi(r, z, t) = R_1(r) \exp[-\mu_t z + \zeta t],$$

with R_1 being a solution to the second-order ODE in (14), with nonconstant coefficients, with parameter $\beta_1 = \beta_1(\zeta)$ verifying (A.2).

For $r_i < r \leq r_o$, we seek a function in the form

$$\phi(r, z, t) = R_2(r) \exp[-\mu_t z + \zeta t],$$

with R_2 being constituted by Bessel functions with parameter β_2 such that

$$\beta_2 = \left(\zeta/\nu + \mu_a^{(o)} \right) / D^{(o)} - (\mu_t^{(i)})^2 \quad \text{for } o = \text{outer}.$$

Considering (A.2), β_2 reads

$$\beta_2(\zeta) = \begin{cases} \mu_a^{(o)} / D^{(o)} - (\mu_t^{(i)})^2 & \text{if } \zeta = 0 \\ \left(D^{(i)} \beta_1 + (D^{(i)} - D^{(o)}) (\mu_t^{(i)})^2 - \mu_a^{(i)} + \mu_a^{(o)} \right) / D^{(o)} & \text{if } \zeta = \zeta_{\text{in}}. \end{cases} \quad (\text{B.1})$$

B.1. Case $\beta_2 < 0$ (Bessel functions). Using the continuity condition on the function ϕ at $r = r_i$, we have

$$R_2(r) = C_2 J_0(\sqrt{|\beta_2|r}) + \frac{R_1(r_i) - C_2 J_0(\sqrt{|\beta_2|r_i})}{Y_0(\sqrt{|\beta_2|r_i})} Y_0(\sqrt{|\beta_2|r}), \quad C_2 \in \mathbb{R}.$$

The constant C_2 may be determined by the Robin boundary condition (6), namely

$$C_2 J_1(\sqrt{|\beta_2|r_i}) + \frac{R_1(r_i) - C_2 J_0(\sqrt{|\beta_2|r_i})}{Y_0(\sqrt{|\beta_2|r_i})} Y_1(\sqrt{|\beta_2|r_i}) = -\frac{1}{\sqrt{|\beta_2|}} \frac{D^{(i)}}{D^{(o)}} R_1'(r_i). \quad (\text{B.2})$$

Taking the wronskian relationship (A.5) into account, for $\beta = \sqrt{|\beta_2|} > 0$, we may compute (B.2), concluding

$$C_2 = -\frac{\pi}{2} r_i \left(\frac{D^{(i)}}{D^{(o)}} R_1'(r_i) Y_0(\sqrt{|\beta_2|r_i}) + \sqrt{|\beta_2|} R_1(r_i) Y_1(\sqrt{|\beta_2|r_i}) \right). \quad (\text{B.3})$$

B.2. Case $\beta_2 > 0$ (modified Bessel functions). Using the continuity condition on the function ϕ at $r = r_i$, we have

$$R_2(r) = C_2 I_0(\sqrt{\beta_2}r) + \frac{R_1(r_i) - C_2 I_0(\sqrt{\beta_2}r_i)}{K_0(\sqrt{\beta_2}r_i)} K_0(\sqrt{\beta_2}r), \quad C_2 \in \mathbb{R}.$$

The wronskian relationship for modified Bessel functions (see [32, pages 360 and 375]) is

$$I_1(\beta r) K_0(\beta r) + K_1(\beta r) I_0(\beta r) = \frac{1}{\beta r}. \quad (\text{B.4})$$

Applying (B.4) for $\beta = \sqrt{\beta_2} > 0$, analogously to (B.2)-(B.3), we conclude

$$C_2 = r_i \left(\frac{D^{(i)}}{D^{(o)}} R_1'(r_i) K_0(\sqrt{\beta_2}r_i) + \sqrt{\beta_2} R_1(r_i) K_1(\sqrt{\beta_2}r_i) \right).$$

REFERENCES

- [1] A. Banerjee, A.A. Ogale, C. Das, K. Mitra, and C. Subramanian. Temperature distribution in different materials due to short pulse laser irradiation. *Heat Transfer Eng.*, 26(8):41–49, 2005.
- [2] S.M. Boronyak and W.D. Merryman. Development of a simultaneous cryo-anchoring and radiofrequency ablation catheter for percutaneous treatment of mitral valve prolapse. *Ann. Biomed. Eng.*, 40(9):1971–1981, 2012.
- [3] A. Capart, S. Ikegaya, E. Okada, M. Machida, and Y. Hoshi. Experimental tests of indicators for the degree of validness of the diffusion approximation. *J. Phys. Commun.*, 5(025012), 2021.
- [4] S.A. Carp, S.A. Prahl, and V. Venugopalan. Radiative transport in the delta- P_1 approximation: Accuracy of fluence rate and optical penetration depth predictions in turbid semi-infinite media. *J. Biomed. Optics*, 9(3):632–647, 2004.
- [5] J. Chiang, S. Birla, M. Bedoya, D. Jones, J. Subbiah, and C.L. Brace. Modeling and validation of microwave ablations with internal vaporization. *IEEE Trans. Biomed. Eng.*, 62(2):657–663, 2015.
- [6] L. Consiglieri. Continuum models for the cooling effect of blood flow on thermal ablation techniques. *Int. J. Thermophys.*, 33(5):864–884, 2012.
- [7] L. Consiglieri. An analytical solution for a bio-heat transfer problem. *Int. J. Bio-Sci. Bio-Technol.*, 5(5):267–278, 2013.

- [8] L. Consiglieri. Analytical solutions in the modeling of the local RF ablation. *J. Mech. Med. Biol.*, 16(05):1650071, 2016.
- [9] L. Consiglieri. Analytical solutions in the modelling of the endovenous laser ablation. *Rev. Acad. Colomb. Ciencias Exactas Fis. Nat.*, 48(187):254–270, 2024.
- [10] L. Consiglieri, I. Dos Santos, and D. Haemmerich. Theoretical analysis of the heat convection coefficient in large vessels and the significance for thermal ablative therapies. *Phys. Med. Biol.*, 48(24):4125–4134, 2003.
- [11] J.W. Jr. Durkee, P.P. Antich, and C.E. Lee. Exact solutions to the multiregion time-dependent bioheat equation. I: Solution development. *Phys. Med. Biol.*, 35(7):847–867, 1990.
- [12] J. Dutta and B. Kundu. An improved analytical model for heat flow in cancerous tumours to avoid thermal injuries during hyperthermia. *Proc. Inst. Mech. Eng. H*, 235(5):500–514, 2021.
- [13] G. D’Alessandro, P. Tavakolian, and S. Sfarra. A review of techniques and bio-heat transfer models supporting infrared thermal imaging for diagnosis of malignancy. *Appl. Sci.*, 2024(14), 2024.
- [14] Y Fan, L Xu, S Liu, J Li, J Xia, X Qin, Y Li, T Gao, and X Tang. The state-of-the-art and perspectives of laser ablation for tumor treatment. *Cyborg Bionic Syst.*, 5:0062, 2024.
- [15] W. Franco, J. Liu, G.X. Wang, J.S. Nelson, and G. Aguilar. Radial and temporal variations in surface heat transfer during cryogen spray cooling. *Phys. Med. Biol.*, 50(2):387, 2005.
- [16] A. González-Suárez, J.J. Pérez, R.M. Irastorza, A. D’Avila, and E. Berjano. Computer modeling of radiofrequency cardiac ablation: 30 years of bioengineering research. *Comput. Methods Programs Biomed.*, 214:106546, 2022.
- [17] Z. Guo and K.H. Kim. Ultrafast laser radiation transfer in heterogeneous tissues with the discrete ordinate method. *Appl. Opt.*, 42(16):2897–2905, 2003.
- [18] X. He and J.C. Bischof. Quantification of temperature and injury response in thermal therapy and cryosurgery. *Crit. Rev. Biomed. Eng.*, 31(5 & 6):355–421, 2003.
- [19] C.-S. Ho, K.-C. Ju, T.-Y. Cheng, Y.-Y. Chen, and W.-L. Lin. Thermal therapy for breast tumors by using a cylindrical ultrasound phased array with multifocus pattern scanning: A preliminary numerical study. *Phys. Med. Biol.*, 52:4585–4599, 2007.
- [20] S.L. Jacques. Optical properties of biological tissues: A review. *Phys. Med. Biol.*, 58:R37–R61, 2013.
- [21] M.K. Jaunich, S. Rajee, K. Kim, K. Mitra, and Z. Guo. Bio-heat transfer analysis during short pulse laser irradiation of tissues. *Int. J. Heat Mass Transf.*, 51:5511–5521, 2008.
- [22] M. Kumar and K.N. Rai. Three phase bio-heat transfer model in three-dimensional space for multiprobe cryosurgery. *J. Therm. Anal. Calorim.*, 147(24):14491–14507, 2022.
- [23] A. Lazarovich, V. Viswanath, A.S. Dahmen, and A. Sidana. A narrative clinical trials review in the realm of focal therapy for localized prostate cancer. *Transl. Cancer Res.*, 13(11):6529–6539, 2024.
- [24] H. Liu, D.A. Boas, Y. Zhang, A.G. Yodh, and B. Chance. Determination of optical properties and blood oxygenation in tissue using continuous NIR light. *Phys. Med. Biol.*, 40(11):1983–1993, 1995.
- [25] J. Liu, X. Chen, and L.X. Xu. New thermal wave aspects on burn evaluation of skin subjected to instantaneous heating. *IEEE Trans. Biomed. Eng.*, 46(4):420–428, 1999.
- [26] B.R. Loiola, H.R.B. Orlande, and G.S. Dulikravich. Thermal damage during ablation of biological tissues. *Numer. Heat Transf. A*, 73(10):685–701, 2018.
- [27] G. Manenti, T. Perretta, M. Nezzo, F.R. Fraioli, B. Carreri, P.E. Gigliotti, A. Micillo, A. Malizia, D. Di Giovanni, C.P. Ryan, and F.G. Garaci. Transperineal Laser Ablation (TPLA) treatment of focal low-intermediate risk prostate cancer. *Cancers*, 16(1404), 2024.
- [28] M.-F. Marqa, P. Colli, P. Nevoux, S.R. Mordon, and N. Betrouni. Focal Laser Ablation of prostate cancer: Numerical simulation of temperature and damage distribution. *BioMed. Eng. OnLine*, 10(45), 2011.

- [29] S. Mordon, B. Buys, J.M. Brunetaud, and Y. Moschetto. New directions in medical laser concept: role of laser-tissue interaction modelization and feedback control. *Lasers Med. Sci.*, 4(Suppl 1):317–327, 1989.
- [30] M.H. Niemz. *Laser-tissue interactions: Fundamentals and applications*. Springer-Verlag, 2007.
- [31] J.T. Oden, K.R. Diller, C.Bajaj, J.C. Browne, J. Hazle, I.Babuška, J. Bass, L. Bidual, L. Domkowicz, A. Elliott, Y. Fang, D. Fuentes, S. Prudhomme, M.N. Rylander, R.J. Stafford, and Y. Zhang. Dynamic data-driven finite element models for laser treatment of cancer. *Numer. Methods Partial Differ. Equ.*, 23(4):904–922, 2007.
- [32] F.W.J. Olver. *Bessel functions of integer order*, chapter 9, pages 355–389. United States Department of Commerce, Washington, D.C., 1972.
- [33] M.N. Özisik. *Heat conduction*. John Wiley & Sons, Ltd, 2012.
- [34] A. Paul, N.K. Bandaru, A. Narasimhan, and S.K. Das. Subsurface tumor ablation with near-infrared radiation using intratumoral and intravenous injection of nanoparticles. *Int. J. Micro-Nano Scale Transport*, 5(2):69–80, 2014.
- [35] S.A. Prahl. *The diffusion approximation in three dimensions*, chapter 7, pages 207–231. Springer US, Boston, MA, 1995.
- [36] A.E.B. Pupo, M.M. González, L.E.B. Cabrales, J.B. Reys, E.J.R. Oria, J.J.G. Nava, R.P. Jiménez, F.M. Sánchez, H.M.C. Ciria, and J.M.B. Cabrales. 3d current density in tumors and surrounding healthy tissues generated by a system of straight electrode arrays. *Math. Comput. Simulation*, 138:49–64, 2017.
- [37] M. Putzer, G.R. da Silva, K. Michael, N. Schröder, T. Schudeleit, M. Bambach, and K. Wegener. Geometrical modeling of ultrashort pulse laser ablation with redeposition and analysis of the influence of spot size and shape. *Mater. Des.*, 246:113357, 2024.
- [38] M.N. Rylander, Y. Feng, J. Bass, and K.R. Diller. Thermally induced injury and heat shock protein expression in cells and tissues. *Ann. N.Y. Acad. Sci.*, 1066:222–242, 2005.
- [39] M.N. Rylander, Y. Feng, K. Zimmermann, and K.R. Diller. Measurement and mathematical modeling of thermally induced injury and heat shock protein expression kinetics in normal and cancerous prostate cells. *Int. J. Hyperth.*, 26(8):748–764, 2010.
- [40] J.L. Sandell and T.C. Zhu. A review of *in-vivo* optical properties of human tissues and its impact on PDT. *J. Biophotonics*, 4(11-12):773–787, 2011.
- [41] E. Schena, P. Saccomandi, and Y. Fong. Laser Ablation for cancer: Past, present and future. *J. Funct. Biomater.*, 8(2), 2017.
- [42] W.M. Star. *Diffusion theory of light transport*, chapter 6, pages 131–206. Springer US, New York, 1995.
- [43] D.W. Tang and N. Araki. On non-Fourier temperature wave and thermal relaxation time. *Int. J. Thermophys.*, 18(2):493–504, 1997.
- [44] E. De Vita, M. De Landro, C. Massaroni, A. Iadicicco, P. Saccomandi, E. Schena, and S. Campopiano. Fiber optic sensors-based thermal analysis of perfusion-mediated tissue cooling in liver undergoing laser ablation. *IEEE Trans. Biomed. Eng.*, 68(3), 2021.
- [45] R.K. Voeller, R.B. Schuessler, and R.J. Damiano Jr. *Surgical treatment of atrial fibrillation*, chapter 59, pages 1375–1394. McGraw-Hill, New York, 2008.
- [46] A. Vogel and V. Venugopalan. *Pulsed Laser Ablation of soft biological tissues*, chapter 14, pages 551–615. Springer Science+Business Media B.V., 2011.
- [47] J. Wang, S. Wu, Z. Wu, H. Gao, and S. Huang. Influences of blood flow parameters on temperature distribution during liver tumor microwave ablation. *Front. Biosci.-Landmark*, 26(9):504–516, 2021.
- [48] P. Whiting, J.M. Dowden, P.D. Kapadia, and M.P. Davis. A one-dimensional mathematical model of laser induced thermal ablation of biological tissue. *Lasers Med. Sci.*, 7:357–368, 1992.

LUISA CONSIGLIERI, INDEPENDENT RESEARCHER PROFESSOR, EUROPEAN UNION

URL: <https://sites.google.com/site/luisaconsiglieri>